www.sciencemag.org/cgi/content/full/science.aat5522/DC1

Supplementary Materials for

Experimental observation of high thermal conductivity in boron arsenide

Joon Sang Kang, Man Li, Huan Wu, Huuduy Nguyen, Yongjie Hu*

*Corresponding author. Email: yhu@seas.ucla.edu

Published 5 July 2018 on *Science* First Release
DOI: 10.1126/science.aat5522

This PDF file includes:

Materials and Methods

Material synthesis and sample preparation

High-quality single-crystal boron arsenide (BAs) was prepared through chemical vapor transport. To minimize defects and built-in stress introduced by lattice mismatch and thermal expansion, single-crystal cubic boron phosphide (BP) was used as the growth substrate. We previously developed high-quality single-crystal BP and the details for their synthesis and preparation are described in our recent publication (*36*). High-purity boron and arsenic coarse powders (99.9999% purity, from Alfa Aesar) were ground by using mortar and pestle, prior to introduction into a quartz tube at a stoichiometric ratio of 1:2. After we loaded our reaction sources, the quartz tube was evacuated and flame sealed under high vacuum (10^{-5} Torr) before placement into a customized three-zone reaction furnace with a 1083 K hot zone, 1058K center zone and a 1033K cold zone. After 5 weeks at these temperatures, the quartz tube and its content were slowly cooled down to room temperature. These reaction steps were repeated until BAs single crystals of high quality were obtained. For thermal measurements, BAs samples were loaded together with single-crystal cubic boron nitride (BN) and diamond samples (from Element Six) into a cryostat (Janis ST-100 Optical Cryostat, from 4 to 800K) with a precise proportional-integral-derivative (PID) temperature controller (Lakeshore Model 335). Simultaneous thermal conductivity measurements on the three materials with the highest thermal conductivity, i.e. BAs, diamond, and BN, were performed with the time-domain thermoreflectance (TDTR) technique (see Thermal Transport Measurements section below) to guarantee measurement accuracy for high conducting materials, and enable direct comparisons between them to understand the phonon physics. For each measurement temperature, once the set temperature was reached, an additional waiting time of over 30 minutes was added before the

actual thermal measurement was performed to ensure that the samples had reached a complete thermal equilibrium and steady temperature.

Structural Characterizations

1. X-ray diffraction (XRD) measurements

Powder XRD was conducted with a Panalytical X'Pert Pro XRD machine with a Cu Kα radiation source. Samples of BAs crystals were gently separated from the growth substrate and transferred to the zero-diffraction substrate. The diffractometer was operated at 45 kV and 40 mA. After measurement, the diffraction peaks were matched with the material data directory and identified as BAs crystals.

Single-crystal XRD was performed using a Bruker SMART APEX II single-crystal XRD machine equipped with a charge-coupled device (CCD) detector. A single piece of BAs crystal (~50 μm size) was separated from the growth substrate and mounted onto the goniometer stage for measurement. First, the crystal quality was carefully examined by full-angle rotation images. The BAs sample was rotated over 360 degrees under x-ray excitation, while the diffraction data was continuously collected by the CCD detector and subsequently combined into a single plot. The combined rotation images showed that the BAs crystal sample was a single crystal in its entirety. Next, to determine the unit-cell crystal structure and examine the possibility of any crystal twinning and defects, single-crystal XRD data were collected with 0.3 degree of frame width and 60s/frame of exposure time. A Mo Kα radiation source was used for data collection. Following the measurements, the Bruker APEX software was used to determine the lattice constant and crystal structure. The BAs crystal sample demonstrated a perfect zinc-blende FCC crystal structure with a lattice constant of 4.78Å. In combination with the measured diffraction

patterns from each frame, the reciprocal lattice space (*k* space) of the BAs crystal sample was constructed and plotted (Fig. S1). Fig. S1a and S1b show the measured reciprocal lattice of the BAs crystal in the (001) and (010) direction, respectively. After verification of the crystallographic direction in the reciprocal lattice, we concluded that the entire BAs crystal was a homogeneous single-crystal domain without any impurity or lattice twinning.

2. Transmission electron microscopy (TEM) measurement

TEM samples were prepared by using a focused ion beam (FIB) machine (Nova 600, FEI). First, a single piece of BAs crystal was cut by FIB into small size pieces: 8 μm×8 μm×2 μm (width × height × thickness), and placed on top of a TEM grid (PELCO FIB Lift-Out, Ted Pella) with a nanomanipulator. The BAs crystal was further milled by FIB until the sample thickness was thin enough (< 100 nm) to be traversed by the electron beam for effective TEM imaging. After FIB, we used concentrated argon ion beam (Nanomill, model 1040, Fischeone) to clean the BAs sample surface. After cleaning, we took the high angle annular dark field (HAADF) image by using aberration-corrected high-resolution scanning TEM (Grand ARM, JEOL, 300 kV). Atomic-resolution TEM images and their fast Fourier transform images were processed with the Gatan TEM software.

3. Raman spectroscopy

Raman spectra were taken with a Raman microscope (inVia, Renishaw) under laser excitation at 633 nm with a 1800 /mm grating. The laser was polarized and backscattered and the Raman microscope operated with the Leica DM2500 optical system.

Thermal Transport Measurements

TDTR is routinely used to measure the thermal conductivity of a wide range of materials (*14*, *15*, *36*, *43–45*). The details of the TDTR measurements are as follows. A Ti:Sapphire oscillator (Tsunami, Spectra-Physics) generates femtosecond laser pulses (100 fs) at a repetition rate of 80.7 MHz and a central wavelength at 800 nm. The laser pulse is split into pump and probe beams. The pump beam passes through an electro-optic modulator (EOM) with a sine-wave modulation up to 20 MHz and then through a bismuth triborate (BIBO) crystal, where its frequency is doubled to a wavelength of 400 nm. The modulated pump beam heats up the sample surface, creating a sharp temperature rise. The transient temperature decay is monitored by the probe beam, which is delayed with a mechanical delay stage for a sub-picosecond resolution of the temperature decay. The thermal conductivity of a sample is extracted by measuring changes in its reflectance signal with a photodetector connected to a lock-in amplifier. The lock-in amplifier transmits in-phase (V_{in}) and out-phase (V_{out}) reflectance signals. A thin aluminum film (~100 nm) was deposited on top of the sample surface for thermal transduction. The thickness of the Al film was verified by picosecond pulse-echo measurements. Sensitivity analysis is performed to optimize the experimental conditions and ensure the measurement accuracy for high thermal conductivity materials(*36*). Ten experimental measurements are plotted together in Figure S3.

A description of the modeling analysis to extract thermal conductivity is provided below and can be found in details in previous publications(*14*, *15*, *36*, *43–47*). For each measurement, we carefully measured the root-mean-square (RMS) diameter ($1/e^2$ diameter) of the pump and probe beams by using the beam offset method (*45*). The pump beam was swept by a piezo-mirror mount with a step resolution of 0.7 μrad, which is equivalent to 2 nm. We used the in-phase

signal to fit the Gaussian distribution of the laser spot.

The measured signal from the linear time invariant system in the lock-in amplifier is expressed as:

$$Z(\omega_0) = R\sum_{N=-\infty}^{\infty} H(\omega_0 + N\omega_s)\exp(iN\omega_s\tau) \qquad \text{(E1) (see Ref (46))}$$

where R is the constant which includes the thermoreflectance coefficient, the electronics gain. The N, ω_0, ω_s, and τ are the integer, modulation frequency, probe frequency, and time delay. The real part in equation E1, or the in-phase signal, Re[Z(ω_0)], is related to the temperature response from the sample at short delay times. On the other hand, the out-of-phase signal, or the imaginary part of equation E1, Im[Z(ω_0)]), is proportional to the imaginary temperature oscillation.

The transient heat conduction model in cylindrical coordinates is expressed as:

$$\rho C_p \frac{\partial T}{\partial t} = \frac{\kappa}{r}\frac{\partial}{\partial r}\left(r\frac{\partial T}{\partial r}\right) + \kappa\frac{\partial^2 T}{\partial z^2} \qquad \text{(E2)}$$

After Hankel transform and Fourier transform, equation (E2) becomes:

$$\rho C_p i f\overline{T}(\omega) + \kappa k^2\overline{T}(\omega) = \kappa\frac{\partial^2\overline{T}(\omega)}{\partial z^2} \qquad \text{(E3)}$$

where ρ, Cp, and κ are the mass density, specific heat, and thermal conductivity, respectively. Rearrangement of equation E3 leads to:

$$\frac{\partial^2\overline{T}(\omega)}{\partial z^2} = \beta^2\overline{T}(\omega) \qquad \text{(E4)}$$

Thus β is defined as:

$$\beta \equiv \frac{\rho C_p i\omega + \kappa k^2}{\kappa} \qquad \text{(E5)}$$

The thermal response of a sample in a given frequency domain is expressed as:

$$\begin{pmatrix} T_b \\ q_b \end{pmatrix} = \begin{pmatrix} \cosh(\beta d) & -\frac{1}{\kappa\beta}\sinh(\beta d) \\ -\kappa\beta\sinh(\beta d) & \cosh(\beta d) \end{pmatrix} \begin{pmatrix} T_t \\ q_t \end{pmatrix} \qquad \text{(E6) (see Ref (46))}$$

where T_b, T_t, q_b, and q_t are temperatures of bottom and top sides, heat flux of bottom and top side, and d is the layer thickness. For multi-layers:

$$\begin{pmatrix} T_b \\ q_b \end{pmatrix} = K_n K_{n-1} K_{n-2} \ldots K_1 \begin{pmatrix} T_t \\ q_t \end{pmatrix} = \begin{pmatrix} a_{11} & a_{12} \\ a_{21} & a_{22} \end{pmatrix} \begin{pmatrix} T_t \\ q_t \end{pmatrix} \qquad \text{(E7)}$$

In the semi-infinite n-th layer:

$$T_t = -\frac{a_{22}}{a_{21}} q_t \qquad \text{(E8)}$$

Heat flux at the top boundary surface is expressed by the Hankel transform of the Gaussian distribution of the beam spot which is:

$$q_t = \frac{A_0}{2\pi}\exp\left(\frac{-k^2 w^2}{8}\right) \qquad \text{(E9)}$$

where A_0 and w are the laser power and radius of beam. By taking the inverse Hankel transform of equation (E8) with the weight average by co-axial probe beam, the frequency domain solution of H in equation E1 is expressed as:

$$H(\omega) = \frac{A}{2\pi}\int_0^\infty \frac{-a_{22}}{a_{21}}\exp\left(-\frac{k^2(w_{pump}^2 + w_{probe}^2)}{8}\right) k\,dk \qquad \text{(E10) } \textit{(see Ref. (46))}$$

The derivations and thermal modeling analysis can be found in more details elsewhere (*7, 8*).

Specific Heat Measurement

The specific heat of boron arsenide was measured using the differential scanning calorimetry (PerkinElmer DSC 8000) across the temperature range from 300K to 600 K. The two

furnaces and the StepScan mode of this machine enable the precise specific heat measurement. During each measurement, there are two crimped aluminum pans scanned across the desired temperature range, in one of which the sample was loaded while the other one was empty. The difference of heat flux through the two pans is used to calculate the thermal energy required by our boron arsenide sample to elevate its temperature. Before each measurement run, a background run was performed in advance to eliminate the measurement errors of heat flux brought by the system itself. The DSC machined was calibrated with aluminum first. We performed the temperature scanning with the heating rate of 10 K/min, temperature interval of 10 K and thermalization time of 1 min under the nitrogen purge flow rate of 20 mL/min.

For mass density, we experimentally measured the lattice constant of BAs sample to be 4.78 Å using single crystal x-ray diffraction (Figure 1f in the main text and Figure S1 in the Supplement information). Considering the crystal structure and unit cell volume so we obtained the mass density is 5.214 g/cm^3.

Crystal stability of BAs

To evaluate the stabilities of BAs crystals(*48*), we measure the thermal conductivity of our BAs crystal after 10 month from its growth. We keep our sample in the atmosphere condition (300K, 1atm, and ~ 60% of relative humidity). We found that there is no degradation in the thermal conductivity of BAs, indicating that BAs crystal is stable in the air up to 10 month. Furthermore, we confirmed temperature stability of our BAs crystal. We heat up our crystal up to 600K in the vacuum and cooling down to room temperature. We repeat the temperature cycle twice and the measured thermal conductivity remains the same. These indicate that BAs crystal is stable under these conditions.

Ab initio Calculation to Evaluate the Effect of Point Defects

We performed ab initio calculation to consider the effect of arsenic vacancy defects at different temperatures (*T)*, following the settings in recent literature (*8*, *18*, *32*). The nonequilibrium phonon distribution function n_λ under an applied temperature gradient can be described by the Boltzmann transport equation (BTE) as

$$\mathbf{v}_\lambda \cdot \nabla T \frac{\partial n_\lambda}{\partial T} = \left(\frac{\partial n_\lambda}{\partial t}\right)_{collisions} \quad \text{(E11)}$$

where $\lambda \equiv (\mathbf{q}, p)$ labels the phonon mode with wave vector $\mathbf{q}$ and polarization p, and $\mathbf{v}_\lambda$ is the phonon group velocity. In Eq. (E11), the phonon drift due to temperature gradient on the left side is balanced by the phonon scattering on the right side. The scattering term on the right side of the equation includes intrinsic phonon-phonon scattering and phonon-isotope/defect scattering,

$$\left(\frac{\partial n_\lambda}{\partial t}\right)_{collisions} = \left(\frac{\partial n_\lambda}{\partial t}\right)_{intrinsic} + \left(\frac{\partial n_\lambda}{\partial t}\right)_{defect} \quad \text{(E12)}$$

For phonon scattering due to isotopes or point defects, a perturbation to Hamiltonian due to mass disorder is considered. Using Fermi's golden rule, the phonon-isotope/defect scattering term (*49*) in BTE is expressed as

$$\left(\frac{\partial n_\lambda}{\partial t}\right)_{defect} = \frac{\pi}{2N}\omega_\lambda^2 \sum_{\lambda'} \delta(\omega_\lambda - \omega_{\lambda'}) \sum_b g(b) |\mathbf{e}_{\lambda'}^*(b) \cdot \mathbf{e}_\lambda(b)|^2 \left[n_\lambda(n_{\lambda'} + 1) - n_{\lambda'}(n_\lambda + 1)\right] \quad \text{(E13)}$$

where ω_λ is the angular frequency of phonon mode λ, $\mathbf{e}_\lambda(b)$ is the vibrational eigenvector of the b^{th} atom in unit cell and phonon mode λ, and N is the number of unit cells in the crystal. $g(b)$ is a factor that describes the mass variance of the b^{th} atom in unit cell,

$$g(b) = \sum_i f_i(b) \left[1 - \frac{M_i(b)}{\bar{M}(b)}\right]^2 \quad \text{(E14)}$$

where $f_i(b)$ and $M_i(b)$ are the fraction and the atomic mass of the i^{th} isotope of the b^{th} atom respectively, and $\bar{M}(b)$ is the average atomic mass of the element of the b^{th} atom. Arsenic

vacancies are treated as an isotope to arsenic with zero mass. In this method, the changes of interatomic potential are ignored, whose influence to lattice thermal conductivity is negligible at low vacancy concentration (< 0.01%) (*32*). For the calculation of Figure 2d in this paper, we used a vacancy concentration ~ 0.002% to match the calculated thermal conductivity with the measured value at room temperature. The calculated curve (green dashed line, Figure 2d) represents the prediction of temperature-dependent thermal conductivity when three-phonon process and defect scattering dominate the thermal transport (i.e. four-phonon process is negligible).

According to Eq. (E13), the isotope scattering term is determined by nonequilibrium phonon distribution function n_λ. Similarly, using Fermi's golden rule, phonon-phonon intrinsic scattering term $\left(\frac{\partial n_\lambda}{\partial t}\right)_{intrinsic}$ considering three-phonon process can be expressed as a function of nonequilibrium phonon distribution function and third-order interatomic force constants(*11*, *50*). Hence, the unknown n_λ is on both sides of the BTE. To calculate the thermal conductivity of most common materials, a single mode relaxation time approximation (RTA) is usually applied to derive the phonon lifetime time, and subsequently the thermal conductivity can be derived from kinetic theory(*6*). Within the single mode RTA, the phonon distribution for mode λ' in Eq. (E13) (or mode λ' and λ'' for three phonon process) follows the equilibrium Bose-Einstein distribution, and a perturbation is given to mode λ, so that one can compute the phonon lifetime for mode λ by BTE. However, the single mode RTA approximation can underestimate the thermal conductivity for high thermal conductivity materials such as graphene and diamond (11). This is due to inaccurate treats of the normal phonon-phonon scattering process and the breakdown of the local equilibrium for materials with small phonon scattering rates. Therefore, instead of RTA, we used the iterative solution of BTE (*11*) here to calculate the thermal

conductivity of BAs. For a small temperature gradient (∇T), the nonequilibrium phonon distribution n_λ can be linearly expanded as $n_\lambda = n_\lambda^0 + \left(-\partial n_\lambda^0/\partial T\right)\mathbf{F}_\lambda \cdot \nabla T$, where n_λ^0 is the Bose-Einstein distribution under equilibrium state. $\mathbf{F}_\lambda$ can be derived by iteratively solving the BTE. The lattice thermal conductivity tensor $\kappa^{\alpha\beta}$ can be calculated by summing over all the phonon modes in first Brillouin zone(*11*, *50*),

$$\kappa^{\alpha\beta} = \frac{1}{k_B T^2 \Omega N}\sum_\lambda n_0(n_0+1)(\hbar\omega_\lambda)^2 v_\lambda^\alpha F_\lambda^\beta \qquad \text{(E15)}$$

where $\hbar$ is the Plank constant over 2π, Ω is the volume of unit cell. Here, the first Brillouin zone is discretized by a 28 × 28 × 28 **q** mesh. v_λ^α is the group velocity of phonon mode λ along direction α, which can be calculated from phonon dispersion relation,

$$v_\lambda^\alpha = \frac{\partial\omega}{\partial q^\alpha} \qquad \text{(E16)}$$

where q^α is the wave vector along direction α.

We calculated the second and third order interatomic force constants (IFCs). Second-order IFCs are required for deriving phonon dispersion relation. We obtained second-order IFCs based on density functional theory (DFT) (*51*, *52*) and density functional perturbation theory (DFPT) (*53*) using Quantum ESPRESSO (*54*, *55*) package respectively. In self-consistent calculations of electronic structure using plane-wave basis, we used norm-conserving pseudopotentials under local density approximation for both boron and arsenic (*56*). The kinetic energy cutoff for electronic wavefunctions was set as 80 Ry. The lattice constant of BAs is determined by minimizing the total energy of the system in ground-state. After self-consistent calculations of electronic structure, DFPT was applied to obtain the second-order IFCs. For both DFT and DFPT calculations, we used 6 × 6 × 6 Monkhorst-Pack k-points meshes. Third-order IFCs are required for three phonon process of the intrinsic phonon-phonon scattering. The third-

order IFCs were obtained from a 4 × 4 × 4 supercell with 128 atoms, using finite displacement method in real space. Up to fifth nearest neighbors were considered. A package thirdorder.py (*57*) was used to generate an irreducible set of displacements and then extract third order IFCs from the forces acting on atoms under each displacements. The forces acting on atoms was calculated by DFT. After obtaining the IFCs, the lattice thermal conductivity was computed using ShengBTE package (*50*, *58*).

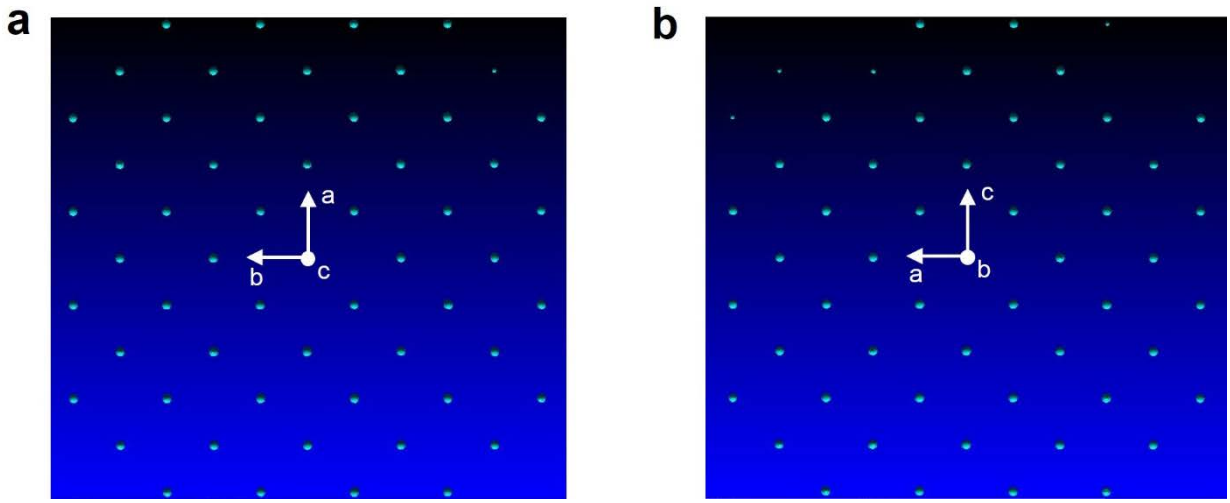

Figure S1. **Verification of the crystal quality of BAs.** The reciprocal lattice of the BAs crystal sample measured from the single-crystal X-ray data for the (001) plane (**a**), (010) plane (**b**), and (100) plane (Figure 1F in the main text), validates that the entire BAs crystal sample is a single-crystal domain without any impurities or lattice twinning.

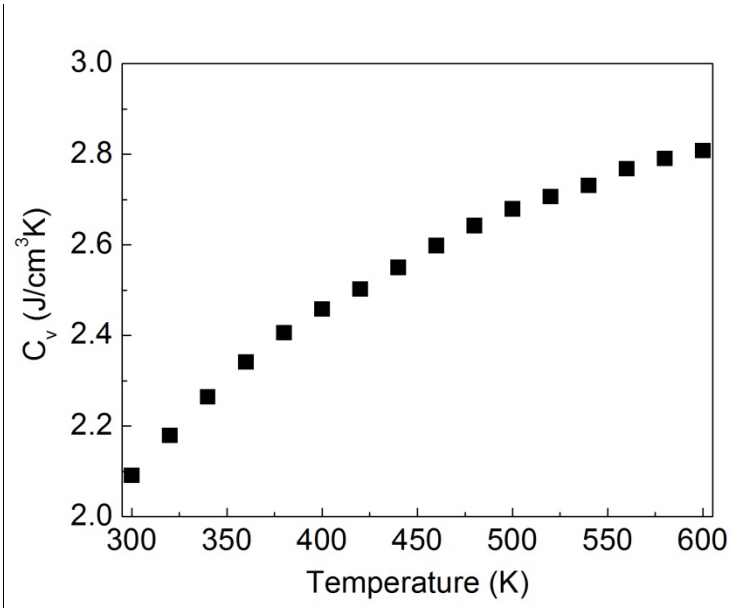

Figure S2. Temperature-dependent volumetric heat capacity of BAs.

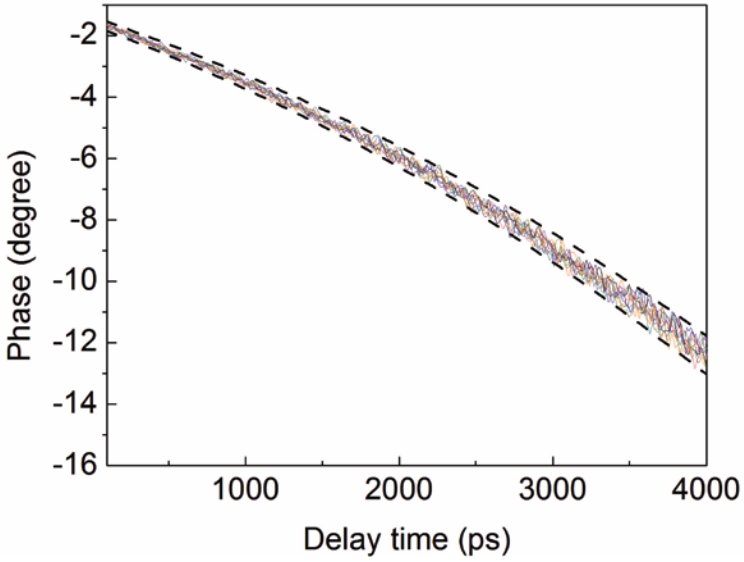

Figure S3. Ten representative TDTR measurement curves (color lines) are shown. The black dashed curves are calculated using the thermal conductivity changed by ±10%.

References and Notes

1. M. M. Waldrop, The chips are down for Moore's law. *Nature* **530**, 144–147 (2016). doi:10.1038/530144a Medline

2. P. Ball, Computer engineering: Feeling the heat. *Nature* **492**, 174–176 (2012). doi:10.1038/492174a Medline

3. S. Chu, A. Majumdar, Opportunities and challenges for a sustainable energy future. *Nature* **488**, 294–303 (2012). doi:10.1038/nature11475 Medline

4. W. L. Arman Shehabi, Sarah Smith, Dale Sartor, Richard Brown, Magnus Herrlin, Jonathan Koomey, Eric Masanet, Nathaniel Horner, Inês Azevedo, United States Data Center Energy Usage Report (2016); https://ses.lbl.gov/publications/united-states-data-center-energy.

5. International Technology Roadmap for Semiconductors, ITRS 2.0 2015 Edition; www.itrs2.net/.

6. J. M. Ziman, *Electrons and Phonons: The Theory of Transport Phenomena in Solids. Oxford Classic Texts in the Physical Sciences* (1960).

7. G. A. Slack, Nonmetallic crystal with high thermal conductivity. *J. Phys. Chem. Solids* **34**, 321–335 (1973). doi:10.1016/0022-3697(73)90092-9

8. L. Lindsay, D. A. Broido, T. L. Reinecke, First-principles determination of ultrahigh thermal conductivity of boron arsenide: A competitor for diamond? *Phys. Rev. Lett.* **111**, 025901 (2013). doi:10.1103/PhysRevLett.111.025901 Medline

9. N. Mingo, D. A. Broido, Lattice thermal conductivity crossovers in semiconductor nanowires. *Phys. Rev. Lett.* **93**, 246106 (2004). doi:10.1103/PhysRevLett.93.246106 Medline

10. N. Mingo, D. A. Broido, Carbon nanotube ballistic thermal conductance and its limits. *Phys. Rev. Lett.* **95**, 096105 (2005). doi:10.1103/PhysRevLett.95.096105 Medline

11. A. Ward, D. A. Broido, D. A. Stewart, G. Deinzer, Ab initio theory of the lattice thermal conductivity in diamond. *Phys. Rev. B* **80**, 125203 (2009). doi:10.1103/PhysRevB.80.125203

12. K. Esfarjani, G. Chen, H. T. Stokes, Heat transport in silicon from first-principles calculations. *Phys. Rev. B* **84**, 85204 (2011). doi:10.1103/PhysRevB.84.085204

13. L. Lindsay, D. A. Broido, T. L. Reinecke, Thermal conductivity and large isotope effect in GaN from first principles. *Phys. Rev. Lett.* **109**, 095901 (2012). doi:10.1103/PhysRevLett.109.095901 Medline

14. M. N. Luckyanova, J. Garg, K. Esfarjani, A. Jandl, M. T. Bulsara, A. J. Schmidt, A. J. Minnich, S. Chen, M. S. Dresselhaus, Z. Ren, E. A. Fitzgerald, G. Chen, Coherent phonon heat conduction in superlattices. *Science* **338**, 936–939 (2012). doi:10.1126/science.1225549 Medline

15. Y. Hu, L. Zeng, A. J. Minnich, M. S. Dresselhaus, G. Chen, Spectral mapping of thermal conductivity through nanoscale ballistic transport. *Nat. Nanotechnol.* **10**, 701–706 (2015). doi:10.1038/nnano.2015.109 Medline

16. T. Feng, L. Lindsay, X. Ruan, Four-phonon scattering significantly reduces intrinsic thermal conductivity of solids. *Phys. Rev. B* **96**, 161201 (2017). doi:10.1103/PhysRevB.96.161201

17. C. Uher, Keeping it cool. *Physics (College Park Md.)* **6**, 76 (2013). doi:10.1103/Physics.6.76

18. D. A. Broido, L. Lindsay, T. L. Reinecke, *Ab initio* study of the unusual thermal transport properties of boron arsenide and related materials. *Phys. Rev. B* **88**, 214303 (2013). doi:10.1103/PhysRevB.88.214303

19. R. M. Wentzcovitch, M. L. Cohen, P. K. Lam, Theoretical study of BN, BP, and BAs at high pressures. *Phys. Rev. B Condens. Matter* **36**, 6058–6068 (1987). doi:10.1103/PhysRevB.36.6058 Medline

20. M. Lax, P. Hu, V. Narayanamurti, Spontaneous phonon decay selection rule: N and U processes. *Phys. Rev. B* **23**, 3095–3097 (1981). doi:10.1103/PhysRevB.23.3095

21. L. Lindsay, D. A. Broido, T. L. Reinecke, Phonon-isotope scattering and thermal conductivity in materials with a large isotope effect: A first-principles study. *Phys. Rev. B* **88**, 144306 (2013). doi:10.1103/PhysRevB.88.144306

22. S. Tamura, Isotope scattering of large-wave-vector phonons in GaAs and InSb: Deformation-dipole and overlap-shell models. *Phys. Rev. B* **30**, 849–854 (1984). doi:10.1103/PhysRevB.30.849

23. J. A. Perri, S. Laplaca, B. Post, New group III–group V Compounds: BP and BAs. *Acta Crystallogr.* **11**, 310 (1958). doi:10.1107/S0365110X58000827

24. F. V. Williams, R. A. Ruehrwein, The preparation and properties of boron phosphides and arsenides. *J. Am. Chem. Soc.* **82**, 1330–1332 (1960). doi:10.1021/ja01491a014

25. J. Osugi, K. Shimizu, Y. Tanaka, Chemical reaction at high temperature and high pressure. II Reaction of boron and arsenic at high temperature and high pressure. *Proc. Jpn. Acad.* **42**, 48 (1966).

26. S. M. Ku, Preparation and properties of boron arsenides and boron arsenide-gallium arsenide mixed crystals. *J. Electrochem. Soc.* **113**, 813 (1966). doi:10.1149/1.2424125

27. A. F. Armington, Vapor transport of boron, boron phosphide and boron arsenide. *J. Cryst. Growth* **1**, 47–48 (1967). doi:10.1016/0022-0248(67)90007-3

28. T. L. Chu, A. E. Hyslop, Crystal growth and properties of boron monoarsenide. *J. Appl. Phys.* **43**, 276–279 (1972). doi:10.1063/1.1661106

29. P. Rudolph, Ed., *Handbook of Crystal Growth, Vol. II, Bulk Crystal Growth* (Elsevier, 2015); http://store.elsevier.com/Handbook-of-Crystal-Growth/isbn-9780444633033/).

30. B. Lv, Y. Lan, X. Wang, Q. Zhang, Y. Hu, A. J. Jacobson, D. Broido, G. Chen, Z. Ren, C.-W. Chu, Experimental study of the proposed super-thermal-conductor: BAs. *Appl. Phys. Lett.* **106**, 074105 (2015). doi:10.1063/1.4913441

31. F. Tian, B. Song, B. Lv, J. Sun, S. Huyan, Q. Wu, J. Mao, Y. Ni, Z. Ding, S. Huberman, T.-H. Liu, G. Chen, S. Chen, C.-W. Chu, Z. Ren, Seeded growth of boron arsenide single

crystals with high thermal conductivity. *Appl. Phys. Lett.* **112**, 031903 (2018). doi:10.1063/1.5004200

32. N. H. Protik, J. Carrete, N. A. Katcho, N. Mingo, D. Broido, Ab initio study of the effect of vacancies on the thermal conductivity of boron arsenide. *Phys. Rev. B* **94**, 045207 (2016). doi:10.1103/PhysRevB.94.045207

33. B. E. Warren, *X-ray Diffraction* (Addison-Wesley, MA, 1969).

34. Materials and methods are available as supplementary materials.

35. D. B. Williams, C. B. Carter, *Transmission Electron Microscopy: A Textbook for Materials Science* (Springer, Boston, MA, 2009).

36. J. S. Kang, H. Wu, Y. Hu, Thermal properties and phonon spectral characterization of synthetic boron phosphide for high thermal conductivity applications. *Nano Lett.* **17**, 7507–7514 (2017). doi:10.1021/acs.nanolett.7b03437 Medline

37. D. G. Onn, A. Witek, Y. Z. Qiu, T. R. Anthony, W. F. Banholzer, Some aspects of the thermal conductivity of isotopically enriched diamond single crystals. *Phys. Rev. Lett.* **68**, 2806–2809 (1992). doi:10.1103/PhysRevLett.68.2806 Medline

38. L. Wei, P. K. Kuo, R. L. Thomas, T. R. Anthony, W. F. Banholzer, Thermal conductivity of isotopically modified single crystal diamond. *Phys. Rev. Lett.* **70**, 3764–3767 (1993). doi:10.1103/PhysRevLett.70.3764 Medline

39. J. R. Olson, R. O. Pohl, J. W. Vandersande, A. Zoltan, T. R. Anthony, W. F. Banholzer, Thermal conductivity of diamond between 170 and 1200 K and the isotope effect. *Phys. Rev. B Condens. Matter* **47**, 14850–14856 (1993). doi:10.1103/PhysRevB.47.14850 Medline

40. A. Maradudin, A. Fein, Scattering of neutrons by an anharmonic crystal. *Phys. Rev.* **128**, 2589–2608 (1962). doi:10.1103/PhysRev.128.2589

41. L. Lindsay, D. A. Broido, Three-phonon phase space and lattice thermal conductivity in semiconductors. *J. Phys. Condens. Matter* **20**, 165209 (2008). doi:10.1088/0953-8984/20/16/165209

42. F. Yang, C. Dames, Mean free path spectra as a tool to understand thermal conductivity in bulk and nanostructures. *Phys. Rev. B* **87**, 035437 (2013). doi:10.1103/PhysRevB.87.035437

43. G. T. Hohensee, R. B. Wilson, D. G. Cahill, Thermal conductance of metal-diamond interfaces at high pressure. *Nat. Commun.* **6**, 6578 (2015). doi:10.1038/ncomms7578 Medline

44. A. Sood, J. Cho, K. D. Hobart, T. I. Feygelson, B. B. Pate, M. Asheghi, D. G. Cahill, K. E. Goodson, Anisotropic and inhomogeneous thermal conduction in suspended thin-film polycrystalline diamond. *J. Appl. Phys.* **119**, 175103 (2016). doi:10.1063/1.4948335

45. J. P. Feser, D. G. Cahill, Probing anisotropic heat transport using time-domain thermoreflectance with offset laser spots. *Rev. Sci. Instrum.* **83**, 104901 (2012). doi:10.1063/1.4757863 Medline

46. A. J. Schmidt, X. Chen, G. Chen, Pulse accumulation, radial heat conduction, and anisotropic thermal conductivity in pump-probe transient thermoreflectance. *Rev. Sci. Instrum.* **79**, 114902 (2008). doi:10.1063/1.3006335 Medline

47. D. G. Cahill, Analysis of heat flow in layered structures for time-domain thermoreflectance. *Rev. Sci. Instrum.* **75**, 5119–5122 (2004). doi:10.1063/1.1819431

48. A. Ektarawong, S. I. Simak, B. Alling, First-principles prediction of stabilities and instabilities of compounds and alloys in the ternary B-As-P system. *Phys. Rev. B* **96**, 024202 (2017). doi:10.1103/PhysRevB.96.024202

49. S. Tamura, Isotope scattering of dispersive phonons in Ge. *Phys. Rev. B* **27**, 858–866 (1983). doi:10.1103/PhysRevB.27.858

50. W. Li, J. Carrete, N. A. Katcho, N. Mingo, B. T. E. Sheng, A solver of the Boltzmann transport equation for phonons. *Comput. Phys. Commun.* **185**, 1747–1758 (2014). doi:10.1016/j.cpc.2014.02.015

51. P. Hohenberg, W. Kohn, Inhomogeneous electron gas. *Phys. Rev.* **136** (3B), B864–B871 (1964). doi:10.1103/PhysRev.136.B864

52. W. Kohn, L. J. Sham, Self-consistent equations including exchange and correlation effects. *Phys. Rev.* **140** (4A), A1133–A1138 (1965). doi:10.1103/PhysRev.140.A1133

53. S. Baroni, S. de Gironcoli, A. Dal Corso, P. Giannozzi, Phonons and related crystal properties from density-functional perturbation theory. *Rev. Mod. Phys.* **73**, 515–562 (2001). doi:10.1103/RevModPhys.73.515

54. P. Giannozzi, S. Baroni, N. Bonini, M. Calandra, R. Car, C. Cavazzoni, D. Ceresoli, G. L. Chiarotti, M. Cococcioni, I. Dabo, A. Dal Corso, S. de Gironcoli, S. Fabris, G. Fratesi, R. Gebauer, U. Gerstmann, C. Gougoussis, A. Kokalj, M. Lazzeri, L. Martin-Samos, N. Marzari, F. Mauri, R. Mazzarello, S. Paolini, A. Pasquarello, L. Paulatto, C. Sbraccia, S. Scandolo, G. Sclauzero, A. P. Seitsonen, A. Smogunov, P. Umari, R. M. Wentzcovitch, QUANTUM ESPRESSO: A modular and open-source software project for quantum simulations of materials. *J. Phys. Condens. Matter* **21**, 395502 (2009). doi:10.1088/0953-8984/21/39/395502 Medline

55. P. Giannozzi, O. Andreussi, T. Brumme, O. Bunau, M. Buongiorno Nardelli, M. Calandra, R. Car, C. Cavazzoni, D. Ceresoli, M. Cococcioni, N. Colonna, I. Carnimeo, A. Dal Corso, S. de Gironcoli, P. Delugas, R. A. DiStasio Jr., A. Ferretti, A. Floris, G. Fratesi, G. Fugallo, R. Gebauer, U. Gerstmann, F. Giustino, T. Gorni, J. Jia, M. Kawamura, H.-Y. Ko, A. Kokalj, E. Küçükbenli, M. Lazzeri, M. Marsili, N. Marzari, F. Mauri, N. L. Nguyen, H.-V. Nguyen, A. Otero-de-la-Roza, L. Paulatto, S. Poncé, D. Rocca, R. Sabatini, B. Santra, M. Schlipf, A. P. Seitsonen, A. Smogunov, I. Timrov, T. Thonhauser, P. Umari, N. Vast, X. Wu, S. Baroni, Advanced capabilities for materials modelling with Quantum ESPRESSO. *J. Phys. Condens. Matter* **29**, 465901 (2017). doi:10.1088/1361-648X/aa8f79 Medline

56. We used the pseudopotentials B.pz-n-kjpaw_psl.0.1.UPF and As.pz-n-kjpaw_psl.0.2.UPF from the Quantum ESPRESSO pseudopotential data base: http://www.quantum-espresso.org/pseudopotentials.

57. W. Li, L. Lindsay, D. A. Broido, D. A. Stewart, N. Mingo, Thermal conductivity of bulk and nanowire $Mg_2Si_xSn_{1-x}$ alloys from first principles. *Phys. Rev. B* **86**, 174307 (2012). doi:10.1103/PhysRevB.86.174307

58. W. Li, N. Mingo, L. Lindsay, D. A. Broido, D. A. Stewart, N. A. Katcho, Thermal conductivity of diamond nanowires from first principles. *Phys. Rev. B* **85**, 195436 (2012). doi:10.1103/PhysRevB.85.195436